Research Article

Nano Research
2024, 17(3): 1114–1122

ISSN 1998-0124 CN 11-5974/O4
https://doi.org/10.1007/s12274-023-5917-2

Electrostatically connected nanoarchitected electrocatalytic films for boosted water splitting

Chao-Peng Wang[1,§], Hao Sun[1,§], Gang Bian[1], Jia-Xi Wang[1], Xixi Pang[1], Guoqi Wang[1], Jian Zhu[1,2,3] (✉), and Xian-He Bu[1,2] (✉)

[1] *School of Materials Science and Engineering, National Institute for Advanced Materials, Nankai University, Tianjin 300350, China*
[2] *Tianjin Key Laboratory of Metal and Molecule-Based Material Chemistry, Nankai University, Tianjin 300350, China*
[3] *Tianjin Key Laboratory for Rare Earth Materials and Applications, Nankai University, Tianjin 300350, China*
[§] *Chao-Peng Wang and Hao Sun contributed equally to this work.*

Received: 27 April 2023 / **Revised:** 31 May 2023 / **Accepted:** 11 June 2023

ABSTRACT

Active sites of two-dimensional (2D) electrocatalysts are often partially blocked owing to their inevitable stacking and hydrophobic polymeric binders in macroscale electrodes, therefore impeding their applications in efficient electrolyzers. Here, using layered double hydroxide (LDH) nanosheets as a model 2D electrocatalyst, we demonstrate that their performance toward water splitting can be boosted when they are electrostatically assembled into an organized structure pillared by hydrophilic polyelectrolytes or nanoparticles in a layer-by-layer (LbL) fashion. In particular, their mass activity on a planar electrode can be as large as 2.267 $mA \cdot \mu g^{-1}$ toward oxygen evolution reaction (OER), when NiFe-LDH nanosheets are electrostatically connected by poly(sodium 4-styrenesulfonate) (PSS), while drop-casted NiFe-LDH nanosheets only have a mass activity of 0.116 $mA \cdot \mu g^{-1}$. In addition, these homogeneous NiFe-LDH nanofilms can be easily deposited on three-dimensional (3D) surfaces with high areas, such as carbon cloths, to serve as practical electrodes with overpotentials of 328 mV at a current density of 100 $mA \cdot cm^{-2}$, and stability for 40 h. Furthermore, Pt nanoparticles can be LbL assembled with NiFe-LDH as bifunctional electrodes for synergistically boosted oxygen and hydrogen evolution reactions (HER), leading to successful overall water splitting powered by a 1.5 V battery. This study heralds the spatial control of 2D nanomaterials in nanoscale precision as an efficient strategy for the design of advanced electrocatalysts.

KEYWORDS

layer-by-layer (LbL) assembly, layered double hydroxides (LDH), two-dimensional (2D) electrocatalysts, oxygen evolution reaction (OER), water splitting

1 Introduction

The rapid exhaustion of fossil fuels along with increasing environmental concerns is propelling the development of clean and renewable energies [1, 2]. Electrocatalysts facilitating oxygen evolution reaction (OER) and hydrogen evolution reaction (HER) play significant roles in the design of energy conversion and storage devices, such as water splitting and metal-air batteries [3–7]. Their catalytic performance is affected by many factors, including particle sizes [8–11], crystallinity [12–14], surface morphology [15–17], catalyst loading [18], and doping [19–23]. Recently, two-dimensional (2D) nanomaterials, such as layered double hydroxide (LDH) or metal dichalcogenides, have emerged as exciting candidates for electrocatalysis, owing to their high surface areas and aspect ratios [24, 25]. However, their active centers cannot be fully accessed owing to the inevitable stacking during their assembly on macroscale electrodes using conventional drop casting methods [26, 27]. Besides, polymer binders, such as Nafion, are usually required to ensure electrocatalysts firmly attaching to the electrode surfaces [28, 29]. Such binders would tend to impede the mass transport and charge transfer during the electrocatalysis due to their insulating nature and hydrophobicity [30]. Moreover, the adhesion dominated by van der Waals forces between electrocatalysts and underlying substrates is sometimes too weak to prevent the active layers from being peeled off in long-term operations, leading to gradual deterioration of performance [31, 32]. Alternatively, growing 2D nanomaterials directly on conductive substrates through hydrothermal/solvothermal strategy can fully expose the active sites and increase stability [33, 34]. However, this growth method depends on the surface of substrates and lacks scalability, thereby limiting its practical industrial application [35, 36]. Therefore, it is desirable to employ a facile strategy to achieve ordered assembly of 2D electrocatalysts on arbitrary conductive substrates for optimized mass activity and durability.

On the basis of these considerations, layer-by-layer (LbL) assembly is considered to be a promising approach to allow regulated deposition of electrocatalysts on desired supporting substrates. This technology represents a feasible yet effective pathway for assembling a myriad of polymers or nanomaterials into multilayer films or hierarchical nanostructures through complementary interactions with nanoscale precision [37, 38].

Address correspondence to Jian Zhu, zj@nankai.edu.cn; Xian-He Bu, buxh@nankai.edu.cn

Having demonstrated its versatility in many applications [39], such as mechanically strong materials, energy storage devices, electronics, LbL assembly has recently emerged as a capable technique in the field of electrocatalysis to enable uniform formation of active coatings [40–42]. In the ordered assembled films, vertically stacked 2D materials with enlarged spacing are expected to get better exposure of active sites with accelerated mass diffusion and facilitated dissipation of gas bubbles during the electrocatalytic process. In particular, its ability to spatially arrange heterogenous nanomaterials into an integrated structure permits the precise design of multiple synergistically interacting interfaces, thereby enhancing catalytic performance beyond individual components [43, 44].

In this work, we propose LbL assembly as a general Nafion-free approach to enable electrostatically connected electrocatalytic films of 2D nanomaterials with enhanced mass activity toward water splitting. As a representative catalyst, ultrathin NiFe LDHs nanosheets were pillared by hydrophilic poly(sodium 4-styrenesulfonate) (PSS) by LbL assembly onto desired conductive substrates (Fig. 1). The thickness of such catalytic films can be meticulously controlled, allowing us to monitor the OER activities per deposition cycle. Benefiting from abundant exposed surface sites, high interface wettability, and enhanced charge transport, the as-obtained NiFe-LDH films exhibit remarkably improved OER performance. Their mass activity can reach 2.267 $mA \cdot \mu g^{-1}$ at an overpotential of 350 mV, which is nearly 19 times higher than that of drop-casted NiFe electrodes. These LDH nanosheets can be further deposited on a porous carbon paper to serve as a practical electrode, demonstrating a low overpotential of 252 mV at 10 $mA \cdot cm^{-2}$ along with prominent durability. Furthermore, a bifunctional electrode capable of OER and HER is composed of alternately stacked NiFe-LDH nanosheets and Pt-C nanoparticles, displaying superior electrocatalytic activities to mechanically mixed composites. The bifunctional electrocatalytic films can function simultaneously as the anode and the cathode for overall water splitting. They require a cell voltage of 1.55 V to yield a current density of 10 $mA \cdot cm^{-2}$, outperforming commercially available RuO_2||Pt-C electrodes.

2 Experimental

2.1 Chemicals

$Ni(NO_3)_2 \cdot 6H_2O$, $Fe(NO_3)_3 \cdot 9H_2O$, and NaOH were purchased from Aladdin Industrial Corporation. PSS (PSS, MW of 70 K), poly(diallyldimethylammonium chloride) (PDDA, MW of 2000–350 K), and formamide were obtained from Sigma-Aldrich. All chemicals are analytical grade and used without further purification. Deionized (DI) water was prepared for all experiments.

2.2 Synthesis of monolayer NiFe-LDH nanosheets

A 20.0 mL aqueous solution composed of 37.5 mM $Ni(NO_3)_2 \cdot 6H_2O$ (0.2181 g) and 12.5 mM $Fe(NO_3)_3 \cdot 9H_2O$ (0.1010 g) was added drop by drop to 20 mL of a 23 vol.% formamide solution with constant stirring at 80 °C. Simultaneously, a 0.25 M NaOH solution was added dropwise to maintain the system at a pH value of ca.10. The reaction was completed within 10 min. After cooling to room temperature, the prepared sample was centrifuged and washed with a mixture of ethanol and water (1:1 by volume) three times, then kept in a wet state for subsequent use.

2.3 Preparation of the LDH nanosheets colloidal dispersion

About 30 mg of the wet LDH-monolayer nanosheets were dispersed in 30 mL of a mixture of ethanol and water (1:1 by volume) and then subjected to ultrasonic (250 W) exfoliation treatment for 30 min. After that, the solution was centrifuged for 5 min at 2000 rpm to remove any residual large LDH-monolayer nanosheets. The top 80% of the solution was decanted for LbL assembly.

2.4 Preparation of the Pt-C dispersion

10 mg Pt-C (10%) and 20 mg sodium cholate were ultrasonicated with a power of 650 W for 30 min in 20 mL of a mixture of ethanol and water (1:1 by volume). The solution was then centrifuged for 5 min at 1000 rpm to remove large particles. The top 80% of the solution with a negative charge was decanted for LbL assembly.

2.5 LbL assembly of NiFe-LDH/PSS multilayer films

NiFe-LDH/PSS multilayer films were assembled onto the gold resonator and carbon paper for the study of electrochemical properties. Firstly, the gold resonator was cleaned in turn in an ultrasonic bath containing deionized water, acetone, ethanol, and deionized water for 10 min each, and then blew it dry with nitrogen. Subsequently, the gold resonator was treated using O_2 plasma with a power of 120 W and the treatment time was 2 min. After these procedures, the surface of substrates was hydrophilic and negatively charged. Two bilayers of PDDA/PSS as precursor layers were first self-assembled on the substrate surface to enhance charge and adsorption capacity, followed by sequential dipping of the device in NiFe-LDH colloidal suspension and PSS solutions (1 $g \cdot L^{-1}$) for 2 min each. Moreover, water washing and nitrogen drying were required after each monolayer assembly to reinforce the interconnection between layers. The cycle was repeated to build the multilayer self-assembled films referred to as $[LDH/PSS]_n$.

NiFe-LDH/PSS multilayer films on carbon paper were prepared by alternatively depositing them onto carbon paper according to the same recipes described above.

2.6 LbL assembly of NiFe-LDH/Pt multilayer films

The fabrication of NiFe-LDH/Pt multilayer films was similar to that described above for NiFe-LDH/PSS multilayer films, except replacing PSS solutions with Pt-C dispersion.

3 Results and discussion

NiFe-LDH nanosheets were prepared by solvothermal reactions (see the Experimental Section in the Electronic Supplementary Material (ESM) for details) [45, 46]. Powder X-ray diffraction (PXRD) spectrum of as-produced NiFe-LDH shows that its peak locations are consistent with those of α-$Ni(OH)_2$ (Fig. S1 in the ESM). Transmission electron microscopy (TEM) image in Fig. 2(a) reveals that NiFe-LDH nanosheets have an ultrathin morphology with a lateral dimension of 25–50 nm. Moreover, the high-resolution TEM (HRTEM) images of NiFe-LDH show distinct lattice fringes, which correspond to the (012) plane (Fig. S2 in the ESM). The average molar ratio of Ni/Fe is calculated to be 2.9:1, as confirmed by energy dispersive X-ray spectroscopy (EDX), which is close to the starting stoichiometry for the synthesis (Fig. S3 in the ESM). Atomic force microscopy (AFM) image also clearly displays sheet morphology (Fig. 2(b)) and the thickness of NiFe-LDH nanosheets are measured to be approximately 1.5 nm (Fig. 2(c)), further verifying the ultrathin nature.

NiFe-LDH nanosheets are positively charged with a zeta potential of 33.5 mV in aqueous dispersion (Fig. 2(d)), and thus can be served as building blocks to assemble with negatively charged polymers, such as PSS. NiFe-LDH and PSS can be

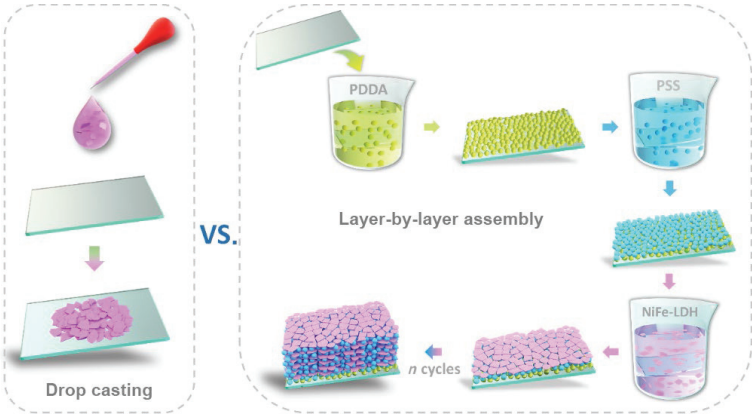

Figure 1 Schematic illustration of LbL assembly versus drop casting for the deposition of electrocatalytic films on conductive substrates.

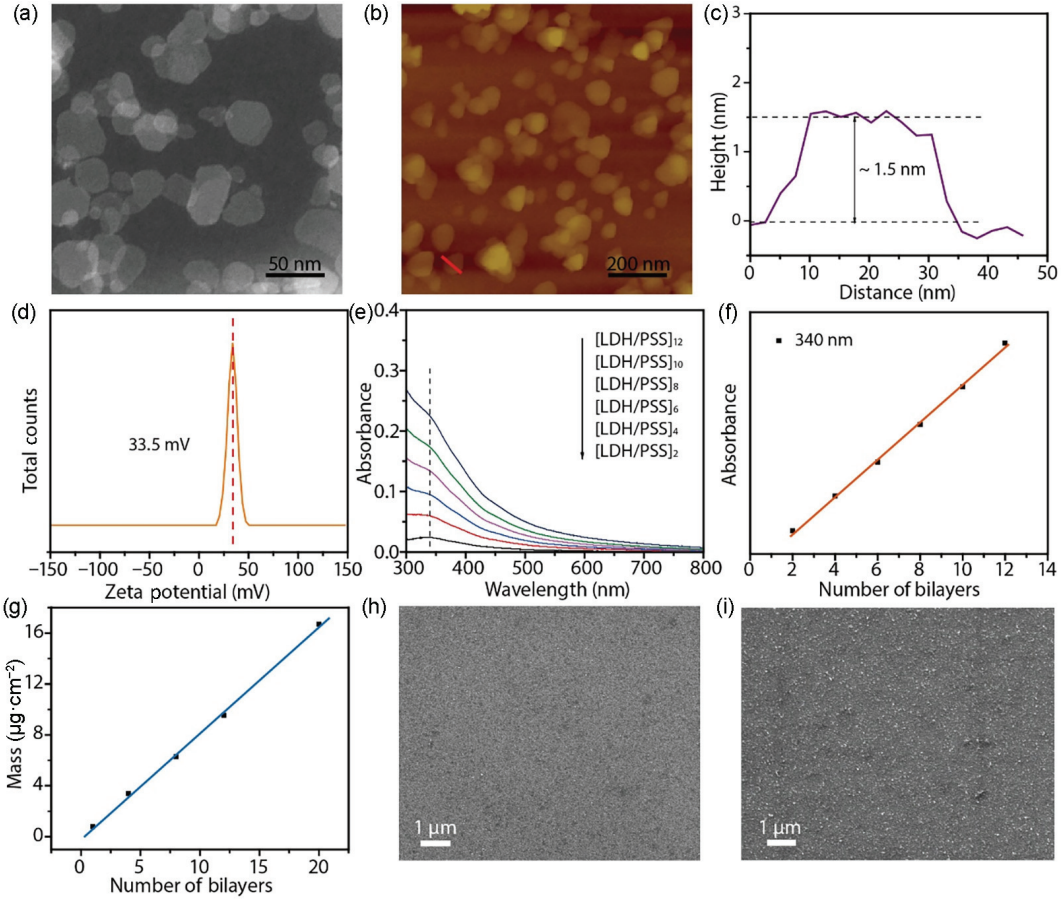

Figure 2 Morphological and structural characterization of NiFe-LDH nanosheets. (a) HAADF-STEM image, (b) AFM image, and (c) the corresponding height profile of NiFe-LDH nanosheets. (d) Zeta-potential of NiFe-LDH aqueous solution. (e) UV–vis spectra of $[LDH/PSS]_n$ (n = 2–12) on glass substrate. (f) The linear relationship between absorbance at 340 nm and bilayer number n. (g) The linear correlation between loading mass measured by QCM and bilayer number n. SEM images of (h) $[LDH/PSS]_1$ and (i) $[LDH/PSS]_8$.

alternatively deposited onto glass slides via LbL assembly with repeating cycles of n (Fig. 1), and their films can thus be denoted as $[LDH/PSS]_n$. Such nanoscale additive process can be monitored by UV–vis absorbance spectra (Fig. 2(e)), in which the absorption peak at 340 nm grows linearly with the increase of bilayer numbers (Fig. 2(f)). This observation implies that an almost equal amount of NiFe-LDH nanosheets are incorporated during a regular deposition procedure. Quartz crystal microbalance (QCM) is also used to monitor the film mass growth during the LBL assembly. It is found that the mass also accumulates in a linear fashion, with a growth rate of 0.81 μg·cm^{-2} per bilayer (Fig. 2(g)). NiFe-LDH nanosheets are uniformly deposited without agglomeration on the substrate, as is confirmed by scanning electron microscope (SEM) image of $[LDH/PSS]_1$ (Fig. 2(h) and Fig. S4(a) in the ESM). When the bilayer numbers increase to 8, a homogeneous film of connected nanosheets is clearly observed in the SEM image (Fig. 2(i) and Fig. S4(b) in the ESM), and its film on the glass substrate also appears to be uniform (Fig. S5 in the ESM). Such morphology is expected to facilitate the effective utilization of each LDH nanosheet and the charge transfer, thereby accelerating electrocatalytic kinetics. As a comparison, NiFe-LDH nanosheets directly drop-casted onto the conductive substrates appear obvious aggregation (Fig. S6 in the ESM).

The influences of thicknesses of the LbL assembled NiFe-LDH films on their electrocatalytic performance are then studied. The $[LDH/PSS]_n$ films on the QCM gold electrodes are measured in 1.0 M KOH solution using a standard three-electrode system. OER activities are significantly enhanced with incremental NiFe-LDH layers, as shown in the scans of linear sweep voltammetry (LSV, Fig. 3(a)). This trend persists until 20 layers, or at a catalyst

loading of 14.8 μg·cm^{-2}, beyond which the electrocatalytic currents are almost unvaried. This observation indicates the availability of more active sites at this stage cannot further improve the electrochemical reaction rate. Enhanced OER activities are also indicated by gradually lowered overpotentials at a current density of 10 mA·cm^{-2} (Fig. 3(b)). The optimal $[LDH/PSS]_{20}$ film requires an overpotential of 282 mV, which is 104 mV lower than that of $[LDH/PSS]_1$. The $[LDH/PSS]_{20}$ also displays a much lower Tafel slope of 57.3 mV·dec^{-1} compared to other thinner films, demonstrating substantially improved catalytic kinetics with the increase of deposited layers (Fig. 3(c)). Furthermore, the electrochemical impedance spectra (EIS) are examined for the interface between the $[LDH/PSS]_n$ and the electrolyte. The related Nyquist plots reveal that a smaller semicircle for $[LDH/PSS]_{20}$ than those of other thinner films, indicating a lower charge transfer resistance during OER (Fig. 3(d)). Specifically, the charge transfer resistances extracted from the impedance spectra for $[LDH/PSS]_n$ are 181.8, 20.4, 7.4, 6.5, and 4.7 Ω, for n = 1, 4, 8, 12, and 20, respectively. Moreover, the active sites of these LbL assembled films can be partially reflected by the area of oxidation peak between 1.3 and 1.48 V relating to the redox-active LDH [18, 47]. From Fig. 3(e), it is observed that the current intensities of these oxidation peaks grow with the increase of sequence layers. Accordingly, the integrated areas under these peaks also rise (Fig. 3(f)), implying that the number of accessible active sites of $[LDH/PSS]_{20}$ is almost 25 times larger than those of $[LDH/PSS]_1$.

As a benchmark, the drop-casted LDH films without any polymer binders on the QCM gold electrodes are prepared to evaluate their OER performance. These films are delineated as LDH-Drop$_m$, where m represents mass loadings in the unit of mg·cm^{-2} of LDH casted on the electrodes. Their OER performances (Fig. 3(g)) are improved with the increase of LDH loadings until an optimal loading of 0.3 mg·cm^{-2}, beyond which the electrocatalytic currents decline. This observation suggests that excessive packing of LDH nanosheets would hinder electron and ion transport with undesired burying of active sites, thus limiting the utilization efficiency of catalysts. In fact, the integrated area of the oxidative peak in the LSV scan (Fig. 3(g)), reflecting the number of active sites, declines from 1.3 × 10^{-5} to 0.61 × 10^{-5} A·V when the loading is increased from 0.3 to 0.4 mg·cm^{-2}. We further study the influence of Nafion binders, conventionally applied to improve the adhesiveness of electrocatalysts, on the OER performance under the optimal mass loading of 0.3 mg·cm^{-2}. It is shown in Fig. 3(h) that the electrochemical currents drop when a merely 0.5 wt.% Nafion is mixed in the LDH films. Further increase of Nafion worsens the OER performance. Specifically, the overpotential at 10 mA·cm^{-2} increases from 309 to 335 and 358 mV, when the Nafion is 0 wt.%, 0.5 wt.%, and 1 wt.%. In addition, Tafel slopes increase remarkably with the addition of Nafion, with LDH-Drop$_{0.3}$ (0% Nafion) showing the lowest Tafel slope of 88.3 mV·dec^{-1} or the fastest reaction kinetics (Fig. 3(i)). This observation is likely owing to the electronically insulating nature of Nafion, together with its high hydrophobicity indicated by its high contact angle over 90° (Fig. S7 in the ESM). It is well-known that surface properties of the surface play an important role in the diffusion of hydroxyl ions and desorption of oxygen gas [48]. In addition, the LDH nanosheets gather together after the introduction of Nafion (Fig. S8 in the ESM), leading to the inaccessibility of active sites. Based on the above analysis, it can be concluded that the usage of Nafion for LDH electrocatalysts slows the OER rate.

A side-by-side comparison is then made between the LbL

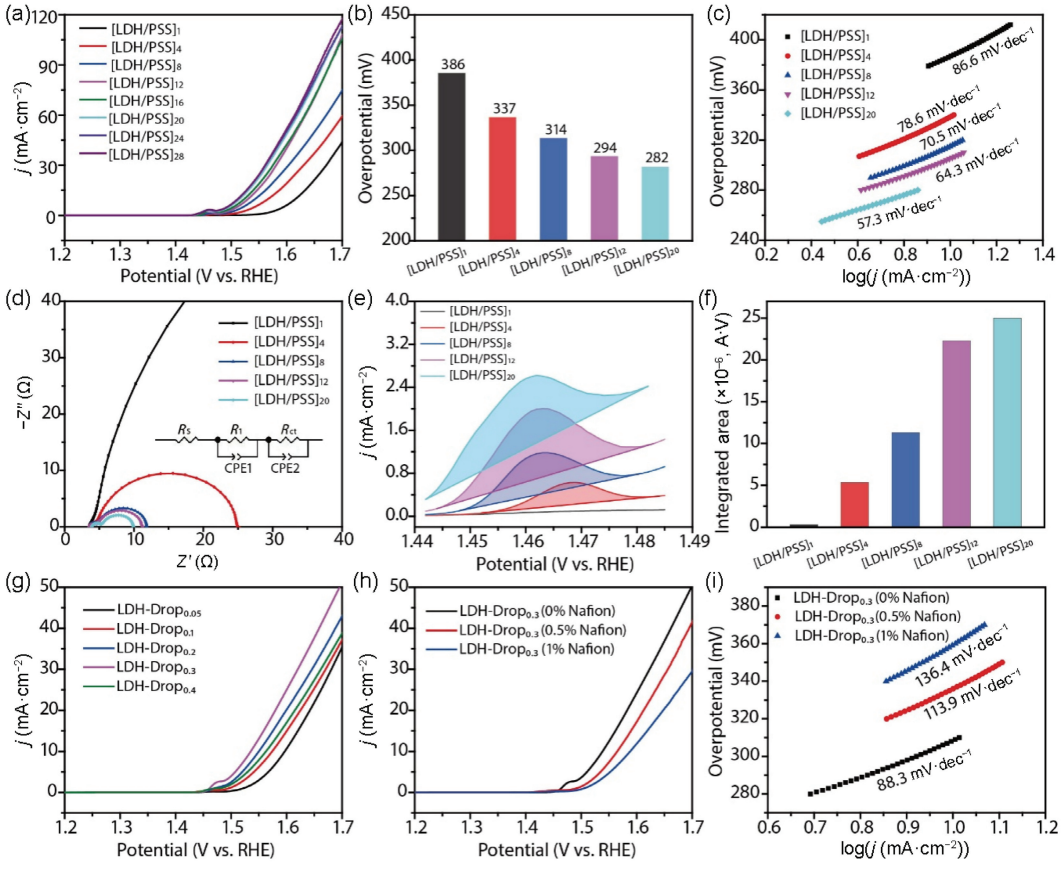

Figure 3 OER performance of NiFe-LDH electrocatalytic films by LbL assembly and drop casting. (a) LSV curves for $[LDH/PSS]_n$. (b) Overpotentials at 10 mA·cm^{-2} for $[LDH/PSS]_n$. (c) Tafel plots derived from the data in (a). (d) EIS curves for $[LDH/PSS]_n$. (e) LSV curves showing the oxidation peak used for area integration. (f) Integrated peak areas for $[LDH/PSS]_n$. (g) LSV curves of LDH-Drop$_m$ without any Nafion. (h) LSV curves and (i) Tafel plots for LDH-Drop$_{0.3}$ with different inclusions of Nafion in the films.

assembled and drop-casted LDH films optimized for OER. Mass activity, defined by the current at a certain overpotential normalized by the mass of catalytic films, is used to evaluate the extent of electrocatalysts accessed during any electrochemical reactions [49]. Remarkably, the mass activity of $[LDH/PSS]_{20}$ reaches 0.877 and 2.267 $mA{\cdot}\mu g^{-1}$ at the overpotentials of 300 and 350 mV respectively, which are much larger than that of LDH-$Drop_{0.3}$ (0% Nafion) (Fig. 4(a)) as well as some of other reported catalysts (Tabel S1 in the ESM). In comparison, the mass activities of LDH-$Drop_{0.3}$ (0% Nafion) are 0.054 and 0.116 $mA{\cdot}\mu g^{-1}$ at the overpotentials of 300 and 350 mV, respectively. Therefore, the LbL assembled LDH films exhibit substantially improved mass activity, or equivalently, the reduced overpotentials with much less loadings of LDH. EIS for both $[LDH/PSS]_{20}$ and LDH-$Drop_{0.3}$ (0% Nafion) films are also compared (Fig. 4(b)). The two semicircles in the Nyquist plots correspond to the interface diffusion impedance in the high frequency region and the charge transfer impedance in low frequency region. Evidently, $[LDH/PSS]_{20}$ exhibits a smaller low-frequency semicircle (4.7 Ω) compared to LDH-$Drop_{0.3}$ (0% Nafion) (5.5 Ω), which indicates a much faster electron transport in the LbL film/electrolyte interface. In addition, the numbers of the exposed catalytic sites for both $[LDH/PSS]_{20}$ and LDH-$Drop_{0.3}$ (0% Nafion) films are collated. These numbers are related to the electrochemically active surface area [50], which can be appraised from the double-layer capacitances (C_{dl}) estimated from cyclic voltammetry [35, 51]. As shown in Fig. 4(c), the calculated C_{dl} of $[LDH/PSS]_{20}$ is 0.39 $mF{\cdot}cm^{-2}$, two times larger than that of LDH-$Drop_{0.3}$ (0% Nafion) (0.18 $mF{\cdot}cm^{-2}$), which implies that LbL films provide larger effective interface areas with the electrolyte. $[LDH/PSS]_{20}$ films also possess larger integrated areas of oxidation peaks in the LSV curves than LDH-$Drop_{0.3}$ (0% Nafion), further supporting more accessible active sites (Fig. 4(d) and Fig. S9 in the ESM).

The PSS pillared between LDH layers in the LbL films provides sufficient free spaces for OER, and is thin enough to avoid the impediment of electron transfer despite its electronically insulating nature. In addition, the PSS is highly hydrophilic, allowing easier adsorption of hydroxyl ions during OER. As presented in Figs. 4(e) and 4(f), the contact angles for LDH-$Drop_{0.3}$ (0% Nafion) and $[LDH/PSS]_{20}$ are 51.4° and 23.1°, respectively, indicating a prominent change in hydrophilicity owing to the addition of PSS. The more hydrophilic nature would effectively strengthen the surface interaction between ions and active sites, thus facilitating adsorption dynamics of the surface species at the LbL film/electrolyte interface.

The limited surface areas of a 2D planar conductive substrate would fundamentally limit the number of accessible active sites of any electrocatalytic films. Therefore, a carbon fiber paper (CFP) is applied as a three-dimensional (3D) porous substrate to further boost current densities of OER, which is required in practical applications. LbL assembly has been a well-known approach to uniformly deposit films on 3D substrates (Fig. 5(a)) [40]. Therefore, NiFe-LDH nanosheets coupled with PSS, i.e., $[LDH/PSS]_n$, are evenly coated on individual carbon fibers using a similar LbL assembly procedure (Fig. 5(b) and Fig. S10 in the ESM). In comparison, drop-casted films, i.e., LDH-$drop_m$, on the CFP display highly aggregated surface morphologies (Fig. 5(c) and Fig. S11 in the ESM). With the increase of thickness, the OER activities of $[LDH/PSS]_n$ gradually improved, and plateaued after 8 cycles when the performance is not limited by the availability of active sites (Fig. 5(d)). The OER activity of $[LDH/PSS]_8$ outperforms other reported representative electrocatalysts (Table S2 in the ESM). The optimal $[LDH/PSS]_8$ on the CFP also possesses the lowest Tafel slope and the smallest charge transfer resistance (Figs. S12(a) and S12(b) in the ESM), implying the unique advantages of ordered stacking structure. Similarly, the OER performance of LDH-$drop_m$ films on the CFP also improves with the loadings of LDH, and almost saturates when the loading is 0.4 $mg{\cdot}cm^{-2}$ (Fig. 5(e)). The side-by-side comparison between the $[LDH/PSS]_8$ and LDH-$drop_{0.4}$ films demonstrates that the LbL assembled film only requires overpotentials of 252 or 287 mV at 10 or 100 $mA{\cdot}cm^{-2}$, much smaller than the drop-casted film (328 or 360 mV, Fig. 5(f)), despite the fact that the $[LDH/PSS]_8$ has much less NiFe-LDH loadings than LDH-$drop_{0.4}$. The superiority of $[LDH/PSS]_8$ is also illustrated by the lower Tafel slope and charge transfer resistance than LDH-$Drop_{0.4}$ (0% Nafion) (Figs. S13(a) and S13(b) in the ESM). The calculated C_{dl} of $[LDH/PSS]_8$ (1.04 $mF{\cdot}cm^{-2}$) is larger than that of LDH-$drop_{0.4}$ (0% Nafion) (0.62 $mF{\cdot}cm^{-2}$), further demonstrating higher intrinsic activity for $[LDH/PSS]_8$ owing to its ordered architecture (Fig. S13(c) in the ESM). Furthermore, the LbL assembled films demonstrate high durability evaluated by chronopotentiometry. As displayed in Fig.

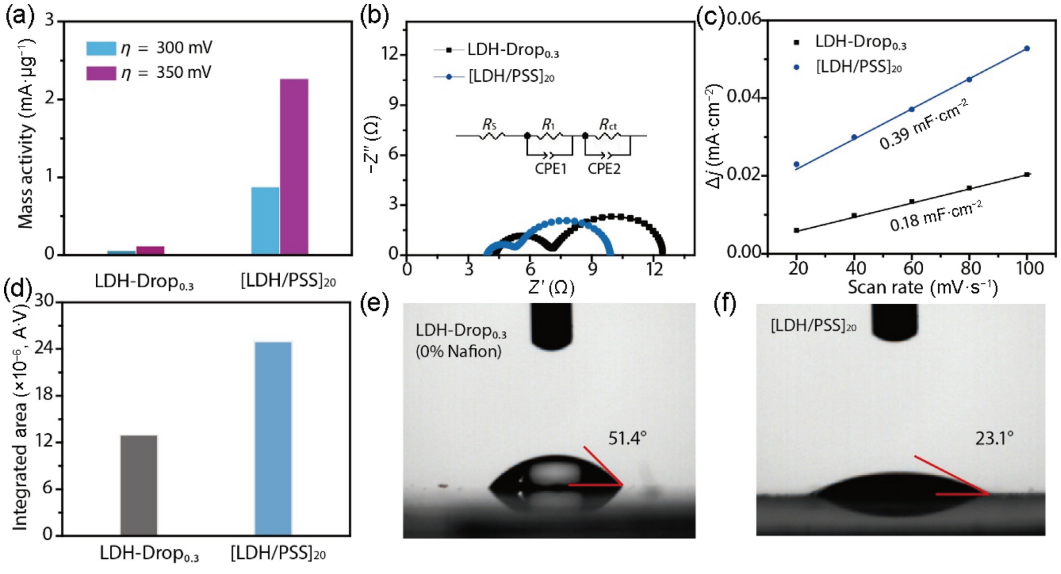

Figure 4 Comparison of OER activities for LbL assembled and drop-casted LDH films. (a) Comparison of OER mass activities of $[LDH/PSS]_{20}$ and LDH-$Drop_{0.3}$ (0% Nafion) at the overpotentials of 300 and 350 mV. (b) EIS curves of LDH-$Drop_{0.3}$ (0% Nafion) and $[LDH/PSS]_{20}$. (c) Double-layer capacitance determined by the current density at different scan rates. (d) Integrated areas of oxidation peaks for LDH-$Drop_{0.3}$ (0% Nafion) and $[LDH/PSS]_{20}$. (e) and (f) Static water contact angles of LDH-$Drop_{0.3}$ (0% Nafion) and $[LDH/PSS]_{20}$.

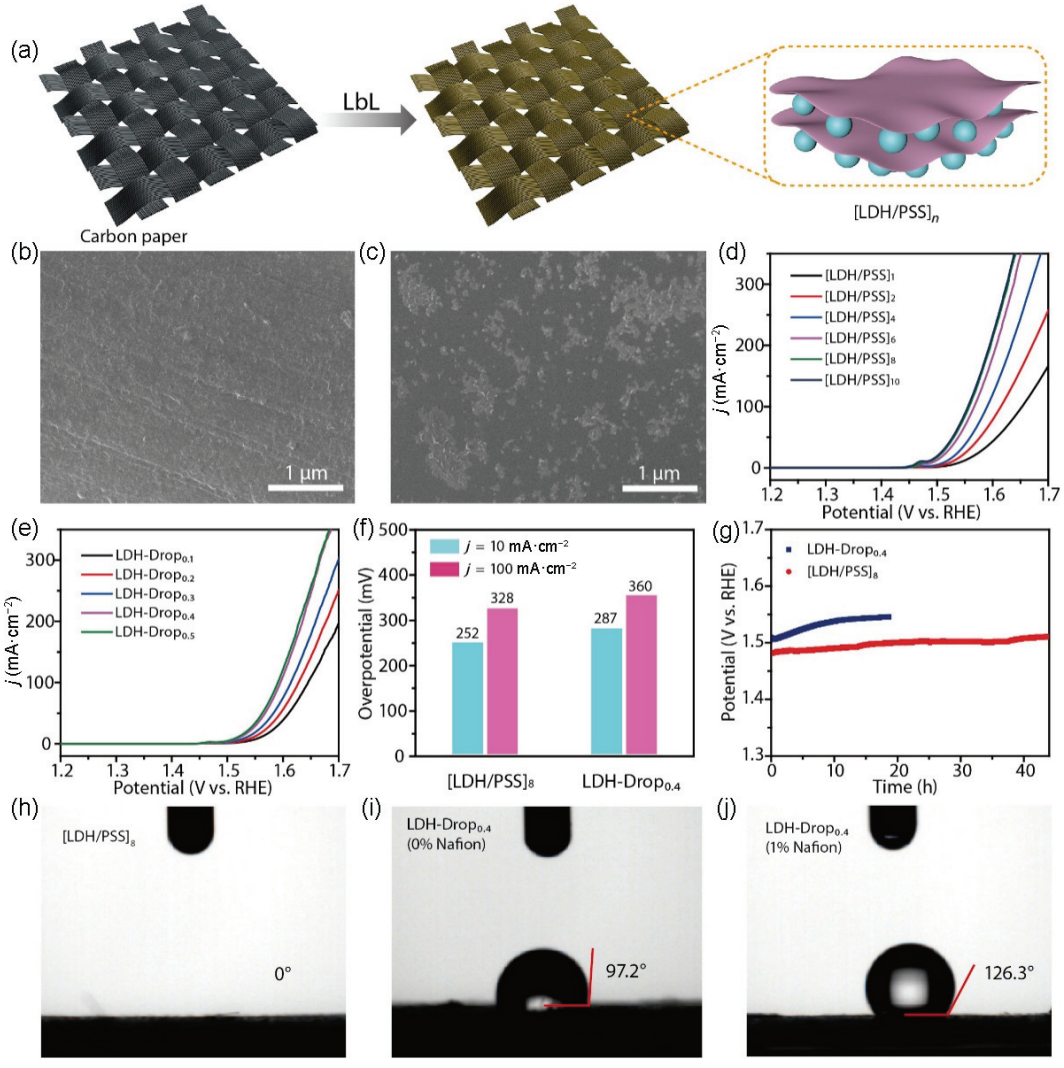

Figure 5 Comparison of OER activities for LbL assembled and drop-casted NiFe-LDH on carbon fiber paper. (a) Schematic representation of LBL assembly for $[LDH/PSS]_n$ on carbon fiber paper. SEM images of (b) $[LDH/PSS]_8$ and (c) LDH-Drop$_{0.4}$ (0% Nafion). LSV curves of (d) $[LDH/PSS]_n$ and (e) LDH-Drop$_m$ (0% Nafion). (f) Overpotentials at 10 and 100 mA·cm^{-2} for $[LDH/PSS]_8$ and LDH-Drop$_{0.4}$ (0% Nafion). (g) Chronopotentiometry curves of $[LDH/PSS]_8$ and LDH-Drop$_{0.4}$ (0% Nafion) at 10 mA·cm^{-2}. (h)–(j) Static water contact angles of $[LDH/PSS]_8$, LDH-Drop$_{0.4}$ (0% Nafion), and LDH-Drop$_{0.4}$ (1% Nafion).

5(g), $[LDH/PSS]_8$ exhibits stable operations for at least 40 h. However, LDH-Drop$_{0.4}$ (0% Nafion) requires higher driving voltages with time increasing, owing to the inevitable delamination of LDH by aggressively formed bubbles during OER.

In addition to the ordered structure, LbL assembled LDH films also demonstrate superhydrophilicity with 0° contact angle (Fig. 5(h)), which is ascribed to the intrinsic hydrophilic properties of LDH and PSS amplified by the uniform 3D porous structures according to the Wenzel model [52]. Such a surface induces more intimate electrolyte/electrocatalysts interfaces, therefore leading to higher OER performance. In comparison, the contact angles of LDH-Drop$_{0.4}$ (0% Nafion) on the mat are 97.2° (Fig. 5(i)). In order to improve the adhesion of drop-casted electrocatalysts on the supporting substrate, Nafion binders are usually required for long-term operation [53]. However, similar to the samples on planar substrates, the addition of Nafion in the drop-casted LDH on the CFP severely limits OER activity (Fig. S14(a) in the ESM). Meanwhile, Tafel slope and resistance associated with the electrochemical reaction kinetics significantly rise with the increase of Nafion dosages (Figs. S14(b) and S14(c) in the ESM). The contact angle of LDH-Drop$_{0.4}$ (1% Nafion) surface is even larger (126.3°), and such hydrophobicity hinders the adsorption dynamics of the surface species (Fig. 5(j)). These results confirm that the usage of Nafion tends to bury active sites of 2D materials and make the interfaces less hydrophilic, leading to inhibited charge transfer and mass transport. On the contrary, LbL assembly can afford well dispersed 2D materials and more hydrophilic interfaces, and provide abundant catalytic sites and rapid charge transfer.

The architecture of LbL assembled films can also be redesigned for bifunctional electrocatalytic properties with enhanced performance by exploiting synergistic interactions between nanolayers. Here, we select commercially available Pt/C particles as one assembling component for accelerating HER. They can be coupled with NiFe-LDH for bifunctional electrocatalytic films capable of HER and OER. The Pt/C particles are dispersed in sodium cholate solution to obtain a uniform dispersion (Fig. S15(a) in the ESM). Pt/C particles are negatively charged with Zeta-potentials of −16.6 mV (Fig. S15(b) in the ESM), and Pt nanocrystals possess a size distribution of ~ 4 nm from TEM analysis (Figs. S16 and S17 in the ESM). They are capable of assembly with positively charged NiFe-LDH nanosheets, as demonstrated by the linear growth of peak intensities at 332 nm for $[LDH/Pt\text{-}C]_n$ (Fig. S18 in the ESM). SEM image and the corresponding element mapping (Fig. S19(a) in the ESM) of $[LDH/Pt\text{-}C]_1$ illustrate a homogeneous distribution of O, Ni, Fe, and Pt, suggesting the intimate mixing of Pt-C and NiFe-LDH

nanosheets. Further increase of layer numbers leads to more dense films with uniformly distributed elements (Fig. S19(b) in the ESM).

In order to further probe the correlation between the layer numbers and electrocatalytic performance, NiFe-LDH and Pt-C are evenly assembled on CFP (Fig. S20 in the ESM). As shown in Fig. S21(a) in the ESM, the onset potentials of $[LDH/Pt\text{-}C]_n$ for OER decrease significantly with the increase of layer numbers, and achieve an optimum performance when n = 8. The $[LDH/Pt\text{-}C]_8$ has an overpotential of 357 mV at 200 mA·cm^{-2}, with a low Tafel plot of 39.9 mV·dec^{-1} (Fig. S21(b) in the ESM). These values are smaller than that of $[LDH/PSS]_8$, owing to the high conductance of Pt/C, which is confirmed by the smaller charge transfer resistance of 2.3 Ω (Fig. S21(c) in the ESM). In addition, the superhydrophilic surface is maintained for $[LDH/Pt\text{-}C]_8$ with contact angles of 0° (Fig. S22 in the ESM). HER activities are also enhanced with the increase of layer number, and the optimum $[LDH/Pt\text{-}C]_{10}$ shows overpotentials of −233 mV at 100 mA·cm^{-2}, Tafel slope of 55.6 mV·dec^{-1} (Volmer–Heyrovsky mechanism) [54], and small charge transfer resistance in the Nyquist plots (Fig. S23 in the ESM).

For comparison, the mechanically mixed NiFe-LDH and Pt-C inks are directly drop-casted on CFP ($LDH_n/Pt\text{-}C_m$, m and n represent the areal loadings in the units of mg·cm^{-2}) for the investigation of their electrochemical properties. As can be seen from Fig. S24 in the ESM, OER activities are positively correlated with the mass loading of NiFe-LDH for $LDH_n/Pt\text{-}C_m$ at the same Pt/C content. However, the increasing Pt-C content inhibits OER activity when NiFe-LDH loading is maintained. Similarly, HER performance is enhanced with the increasing Pt-C loading at the same LDH content, but decreases with more included NiFe-LDH at the same Pt-C content (Fig. S25 in the ESM). By contrast， the $[LDH/Pt\text{-}C]_{10}$ films only need overpotentials of 273 and 320 mV at 20 and 100 mA·cm^{-2} for OER, which are much smaller than that of drop-casted $LDH_{0.4}/Pt\text{-}C_{0.2}$ (302 and 370 mV). Besides, the $[LDH/Pt\text{-}C]_{10}$ films also exhibit lower overpotential of −51 mV for HER at 10 mA·cm^{-2} compared to that of $LDH_{0.2}/Pt\text{-}C_{0.4}$ (−67 mV).

It thus confirms that the direct mixing of NiFe-LDH and Pt/C cannot lead to synergistic enhancement of OER and HER performance. The aggregated networks sacrifice the individual properties of NiFe-LDH and Pt/C likely owing to the inaccessibility of their active sites. In contrast, LbL assembly enables ordered arrangement and efficient coupling interaction, thus achieving mutually optimizing electrocatalytic performance with fully utilized active sites.

We then make a side-by-side comparison between drop-casted and LBL assembled bifunctional electrocatalytic films. $NiFe\text{-}LDH_{0.25}/Pt\text{-}C_{0.25}$ is selected to compare with $[NiFe\text{-}LDH/Pt\text{-}C]_{10}$. Before electrochemical test, a high precision microbalance was used to estimate the mass loadings of $[LDH/Pt\text{-}C]_8$ and $[LDH/Pt\text{-}C]_{10}$, which are estimated to be 0.19 and 0.23 mg·cm^{-2}, respectively, less than 0.5 mg·cm^{-2} of their counterparts in $NiFe\text{-}LDH_{0.25}/Pt\text{-}C_{0.25}$. However, as can be seen in Fig. 6(a), $[LDH/Pt\text{-}C]_8$ shows excellent electrocatalytic activity toward OER with an overpotential of 318 mV at the large current density of 100 mA·cm^{-2}, which is lower than that of $LDH_{0.25}/Pt\text{-}C_{0.25}$ (349 mV). Tafel slopes are determined to be 39.9 and 71.2 mV·dec^{-1} for $[LDH/Pt\text{-}C]_8$ and $LDH_{0.25}/Pt\text{-}C_{0.25}$, respectively, further validating faster catalytic kinetics for $[LDH/Pt\text{-}C]_8$ (Fig. S26(a) in the ESM). Consistently, the $[LDH/Pt\text{-}C]_8$ film has a much smaller charge transfer impedance and larger electrochemical active surface area (ECSA) than the drop-casted $LDH_{0.25}/Pt\text{-}C_{0.25}$ (Figs. S26(b) and S26(c) in the ESM). The $[LDH/Pt\text{-}C]_{10}$ film also displays improved HER properties than $LDH_{0.25}/Pt\text{-}C_{0.25}$. Specifically, the $[LDH/Pt\text{-}C]_{10}$ demonstrates smaller overpotential (260 vs. 350 mV) at 100 mA·cm^{-2} (Fig. 6(b)), lower Tafel slope (55.6 vs. 110.3 mV·dec^{-1}) , larger ECSA (8.24 vs. 6.58 mF·cm^{-2}) , and faster charge transfer (Fig. S27 in the ESM).

Encouraged by the outstanding catalytic performance of $[LDH/Pt\text{-}C]_n$ toward both OER and HER, a two-electrode configuration is assembled using $[LDH/Pt\text{-}C]_n$ as both the anode and cathode for water electrolysis. The benchmarking cell consisting of commercial RuO_2 and Pt/C drop-casted on carbon paper is also measured for comparison. As depicted in Fig. 6(c), the $[LDH/Pt\text{-}C]_8||[LDH/Pt\text{-}C]_{10}$ cell requires a voltage as low as 1.55 V to drive a current density of 10 mA·cm^{-2}, lower than that of $RuO_2||Pt/C$ catalysts (1.64 V) (Table S3 in the ESM). In addition, this cell operates durably, showing no significant degradation after

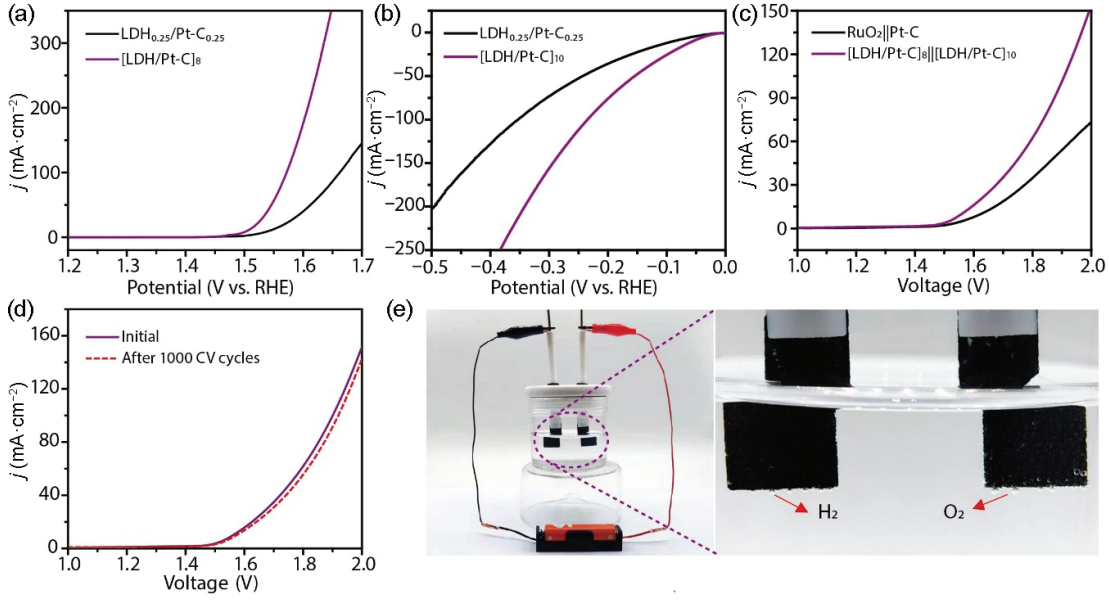

Figure 6 Electrocatalytic properties of bifunctional NiFe-LDH/Pt-C composite films on carbon paper using LbL assembly and drop casting method. (a) Comparison of OER polarization curves for $[LDH/Pt\text{-}C]_8$ and $LDH_{0.25}/Pt\text{-}C_{0.25}$. (b) Comparison of HER polarization curves for $[LDH/Pt\text{-}C]_{10}$ and $LDH_{0.25}/Pt\text{-}C_{0.25}$. (c) Polarization curves of $[LDH/Pt\text{-}C]_8||[LDH/Pt\text{-}C]_{10}$ in a two-electrode water splitting system in 1.0 M KOH. (d) Polarization curves of $[LDH/Pt\text{-}C]_8||[LDH/Pt\text{-}C]_{10}$ for water splitting before and after 1000 CV cycles. (e) Water splitting device driven by a 1.5 V AA battery. Inset: photograph showing the generation of gas bubbles on electrodes.

1000 CV cycles (Fig. 6(d)). The overall water splitting could be powered by a 1.5 V AA-size battery and continuous tiny gas bubbles emerge from the anode and cathode surfaces (Fig. 6(e)).

4 Conclusions

In summary, ultrathin NiFe-LDH nanosheets with ordered stacking and controllable thickness can be homogeneously deposited on the 2D or 3D conductive electrodes with enhanced electrocatalytic performance via LbL assembly. A systematic comparison between LbL assembled and drop-casted films demonstrates the importance of ordered architectures and hydrophilic surfaces for the improved electroactivity. Owing to the fully exposed active site and rapid charge transfer, $[LDH/PSS]_8$ electrode exhibits high mass activity of 2.267 $mA{\cdot}\mu g^{-1}$ at an overpotential of 350 mV toward OER, much larger than similarly performed electrodes reported in literature. Additionally, the controllable combination of NiFe-LDH and Pt-C by LbL assembly provides an approach to designing bifunctional films capable of OER and HER. It is demonstrated that electronic coupling effect between LDH and Pt-C nanolayers synergistically accelerates OER and HER. This cost-effective and scalable LbL assembly approach can guide the development of high-performance electrocatalytic films with minimum mass loadings and multifunctional electrodes for practical electrolyzers.

Acknowledgements

This work was supported by the National Natural Science Foundation of China (NSFC) (Nos. 52273076, 52111540268, and 12004195) and the 111 Project (No. B18030) in China. The authors also acknowledge the financial support by Haihe Laboratory of Sustainable Chemical Transformations (No. YYJC202101) and Open Research Fund Program of the State Key Laboratory of Low Dimensional Quantum Physics (No. KF202113).

Electronic Supplementary Material: Supplementary material (structural characterizations of as-prepared electrode materials, static water contact angle, zeta-potential, and additional performance test) is available in the online version of this article at https://doi.org/10.1007/s12274-023-5917-2.

References

[1] Obama, B. The irreversible momentum of clean energy. *Science* **2017**, *355*, 126–129.

[2] Cheng, W. R.; Xi, S. B.; Wu, Z. P.; Luan, D. Y.; Lou, X. W. *In situ* activation of Br-confined Ni-based metal-organic framework hollow prisms toward efficient electrochemical oxygen evolution. *Sci. Adv.* **2021**, *7*, eabk0919.

[3] He, Y. T.; Yang, X. X.; Li, Y. S.; Liu, L. T.; Guo, S. W.; Shu, C. Y.; Liu, F.; Liu, Y. N.; Tan, Q.; Wu, G. Atomically dispersed Fe-Co dual metal sites as bifunctional oxygen electrocatalysts for rechargeable and flexible Zn-air batteries. *ACS Catal.* **2022**, *12*, 1216–1227.

[4] Sanati, S.; Morsali, A.; García, H. First-row transition metal-based materials derived from bimetallic metal-organic frameworks as highly efficient electrocatalysts for electrochemical water splitting. *Energy Environ. Sci.* **2022**, *15*, 3119–3151.

[5] Wang, C. P.; Feng, Y.; Sun, H.; Wang, Y. R.; Yin, J.; Yao, Z. P.; Bu, X. H.; Zhu, J. Self-optimized metal-organic framework electrocatalysts with structural stability and high current tolerance for water oxidation. *ACS Catal.* **2021**, *11*, 7132–7143.

[6] Wu, Z. X.; Zhao, Y.; Xiao, W. P.; Fu, Y. L.; Jia, B. H.; Ma, T. Y.; Wang, L. Metallic-bonded Pt-Co for atomically dispersed Pt in the Co_4N matrix as an efficient electrocatalyst for hydrogen generation. *ACS Nano* **2022**, *16*, 18038–18047.

[7] Gao, Y. X.; Chen, Z.; Zhao, Y.; Yu, W. L.; Jiang, X. L.; He, M. S.; Li, Z. J.; Ma, T. Y.; Wu, Z. X.; Wang, L. Facile synthesis of MoP-Ru_2P on porous N, P co-doped carbon for efficiently electrocatalytic hydrogen evolution reaction in full pH range. *Appl. Catal. B:Environ.* **2022**, *303*, 120879.

[8] Lv, L.; Yang, Z. X.; Chen, K.; Wang, C. D.; Xiong, Y. J. 2D layered double hydroxides for oxygen evolution reaction: From fundamental design to application. *Adv. Energy Mater.* **2019**, *9*, 1803358.

[9] Liu, D.; Chen, M. P.; Du, X. Y.; Ai, H. Q.; Lo, K. H.; Wang, S. P.; Chen, S.; Xing, G. C.; Wang, X. S.; Pan, H. Development of electrocatalysts for efficient nitrogen reduction reaction under ambient condition. *Adv. Funct. Mater.* **2021**, *31*, 2008983.

[10] Yu, W. L.; Chen, Z.; Fu, Y. L.; Xiao, W. P.; Dong, B.; Chai, Y. M.; Wu, Z. X.; Wang, L. Superb all-pH hydrogen evolution performances powered by ultralow Pt-decorated hierarchical Ni-Mo porous microcolumns. *Adv. Funct. Mater.* **2023**, *33*, 2210855.

[11] Su, H.; Soldatov, M. A.; Roldugin, V.; Liu, Q. H. Platinum single-atom catalyst with self-adjustable valence state for large-current-density acidic water oxidation. *eScience* **2022**, *2*, 102–109.

[12] Kim, Y. J.; Lee, G. R.; Cho, E. N.; Jung, Y. S. Fabrication and applications of 3D nanoarchitectures for advanced electrocatalysts and sensors. *Adv. Mater.* **2020**, *32*, 1907500.

[13] Chen, R.; Hung, S. F.; Zhou, D. J.; Gao, J. J.; Yang, C. J.; Tao, H. B.; Yang, H. B.; Zhang, L. P.; Zhang, L. L.; Xiong, Q. H. et al. Layered structure causes bulk NiFe layered double hydroxide unstable in alkaline oxygen evolution reaction. *Adv. Mater.* **2019**, *31*, 1903909.

[14] Kuai, C. G.; Zhang, Y.; Wu, D. Y.; Sokaras, D.; Mu, L. Q.; Spence, S.; Nordlund, D.; Lin, F.; Du, X. W. Fully oxidized Ni-Fe layered double hydroxide with 100% exposed active sites for catalyzing oxygen evolution reaction. *ACS Catal.* **2019**, *9*, 6027–6032.

[15] Chattot, R.; Bordet, P.; Martens, I.; Drnec, J.; Dubau, L.; Maillard, F. Building practical descriptors for defect engineering of electrocatalytic materials. *ACS Catal.* **2020**, *10*, 9046–9056.

[16] Zhang, X.; Zhao, Y. F.; Zhao, Y. X.; Shi, R.; Waterhouse, G. I. N.; Zhang, T. R. A simple synthetic strategy toward defect-rich porous monolayer NiFe-layered double hydroxide nanosheets for efficient electrocatalytic water oxidation. *Adv. Energy Mater.* **2019**, *9*, 1900881.

[17] Chen, Z.; Li, Q. C.; Xiang, H. M.; Wang, Y.; Yang, P. F.; Dai, C. L.; Zhang, H. D.; Xiao, W. P.; Wu, Z. X.; Wang, L. Hierarchical porous NiFe-P@NC as an efficient electrocatalyst for alkaline hydrogen production and seawater electrolysis at high current density. *Inorg. Chem. Front.* **2023**, *10*, 1493–1500.

[18] Anantharaj, S.; Kundu, S. Do the evaluation parameters reflect intrinsic activity of electrocatalysts in electrochemical water splitting. *ACS Energy Lett.* **2019**, *4*, 1260–1264.

[19] Dou, Y. H.; He, C. T.; Zhang, L.; Yin, H. J.; Al-Mamun, M.; Ma, J. M.; Zhao, H. J. Approaching the activity limit of $CoSe_2$ for oxygen evolution via Fe doping and Co vacancy. *Nat. Commun.* **2020**, *11*, 1664.

[20] Lee, C.; Shin, K.; Jung, C.; Choi, P. P.; Henkelman, G.; Lee, H. M. Atomically embedded Ag via electrodiffusion boosts oxygen evolution of CoOOH nanosheet arrays. *ACS Catal.* **2020**, *10*, 562–569.

[21] Lin, Y. P.; Wang, H.; Peng, C. K.; Bu, L. M.; Chiang, C. L.; Tian, K.; Zhao, Y.; Zhao, J. Q.; Lin, Y. G.; Lee, J. M. et al. Co-induced electronic optimization of hierarchical NiFe LDH for oxygen evolution. *Small* **2020**, *16*, 2002426.

[22] Wu, Z. X.; Yang, P. F.; Li, Q. C.; Xiao, W. P.; Li, Z. J.; Xu, G. R.; Liu, F. S.; Jia, B. H.; Ma, T. Y.; Feng, S. H. et al. Microwave synthesis of Pt clusters on black TiO_2 with abundant oxygen vacancies for efficient acidic electrocatalytic hydrogen evolution. *Angew. Chem., Int. Ed.* **2023**, *62*, e202300406.

[23] Shen, P.; Zhou, B. W.; Chen, Z.; Xiao, W. P.; Fu, Y. L.; Wan, J.; Wu, Z. X.; Wang, L. Ruthenium-doped 3D Cu_2O nanochains as efficient electrocatalyst towards hydrogen evolution and hydrazine oxidation. *Appl. Catal. B:Environ.* **2023**, *325*, 122305.

[24] Zhao, X. H.; Levell, Z. H.; Yu, S.; Liu, Y. Y. Atomistic understanding of two-dimensional electrocatalysts from first principles. *Chem. Rev.* **2022**, *122*, 10675–10709.

[25] Chen, Z. K.; Wang, X. K.; Han, Z. K.; Zhang, S. Y.; Pollastri, S.; Fan, Q. Q.; Qu, Z. Y.; Sarker, D.; Scheu, C.; Huang, M. H. et al. Revealing the formation mechanism and optimizing the synthesis conditions of layered double hydroxides for the oxygen evolution reaction. *Angew. Chem., Int. Ed.* **2023**, *62*, e202215728.
[26] He, Y. Q.; Jia, L. L.; Lu, X. Y.; Wang, C. H.; Liu, X. H.; Chen, G.; Wu, D.; Wen, Z. X.; Zhang, N.; Yamauchi, Y. et al. Molecular-scale manipulation of layer sequence in heteroassembled nanosheet films toward oxygen evolution electrocatalysts. *ACS Nano* **2022**, *16*, 4028–4040.
[27] Sun, H. M.; Yan, Z. H.; Liu, F. M.; Xu, W. C.; Cheng, F. Y.; Chen, J. Self-supported transition-metal-based electrocatalysts for hydrogen and oxygen evolution. *Adv. Mater.* **2020**, *32*, 1806326.
[28] Wang, P. W.; Hayashi, T.; Meng, Q. B.; Wang, Q.; Liu, H.; Hashimoto, K.; Jiang, L. Highly boosted oxygen reduction reaction activity by tuning the underwater wetting state of the superhydrophobic electrode. *Small* **2017**, *13*, 1601250.
[29] Sha, Y.; Peng, Y. D.; Huang, K.; Li, L.; Liu, Z. 3D binder-free integrated electrodes prepared by phase separation and laser induction (PSLI) method for oxygen electrocatalysis and zinc-air battery. *Adv. Energy Mater.* **2022**, *12*, 2200906.
[30] Li, J.; Gao, X.; Li, Z. Z.; Wang, J. H.; Zhu, L.; Yin, C.; Wang, Y.; Li, X. B.; Liu, Z. F.; Zhang, J. et al. Superhydrophilic graphdiyne accelerates interfacial mass/electron transportation to boost electrocatalytic and photoelectrocatalytic water oxidation activity. *Adv. Funct. Mater.* **2019**, *29*, 1808079.
[31] Chen, G. F.; Ma, T. Y.; Liu, Z. Q.; Li, N.; Su, Y. Z.; Davey, K.; Qiao, S. Z. Efficient and stable bifunctional electrocatalysts Ni/Ni_xM_y (M = P, S) for overall water splitting. *Adv. Funct. Mater.* **2016**, *26*, 3314–3323.
[32] Sun, H. M.; Xu, X. B.; Yan, Z. H.; Chen, X.; Jiao, L. F.; Cheng, F. Y.; Chen, J. Superhydrophilic amorphous Co-B-P nanosheet electrocatalysts with Pt-like activity and durability for the hydrogen evolution reaction. *J. Mater. Chem. A* **2018**, *6*, 22062–22069.
[33] Wang, C. P.; Lin, Y. X.; Cui, L.; Zhu, J.; Bu, X. H. 2D metal-organic frameworks as competent electrocatalysts for water splitting. *Small* **2023**, *19*, 2207342.
[34] Lei, H.; Wan, Q. X.; Tan, S. Z.; Wang, Z. L.; Mai, W. J. Pt-quantum-dot-modified sulfur-doped NiFe layered double hydroxide for high-current-density alkaline water splitting at industrial temperature. *Adv. Mater.* **2023**, *35*, 2208209.
[35] Wang, C. P.; Liu, H. Y.; Bian, G.; Gao, X. X.; Zhao, S. C.; Kang, Y.; Zhu, J.; Bu, X. H. Metal-layer assisted growth of ultralong quasi-2D MOF nanoarrays on arbitrary substrates for accelerated oxygen evolution. *Small* **2019**, *15*, 1906086.
[36] Duan, M. T.; Qiu, M. J.; Sun, S. Q.; Guo, X. M.; Liu, Y. J.; Zheng, X. J.; Cao, F.; Kong, Q. H.; Zhang, J. H. Intercalating assembly of NiFe LDH nanosheets/CNTs composite as high-performance electrocatalyst for oxygen evolution reaction. *Appl. Clay Sci.* **2022**, *216*, 106360.
[37] Richardson, J. J.; Björnmalm, M.; Caruso, F. Technology-driven layer-by-layer assembly of nanofilms. *Science* **2015**, *348*, aaa2491.
[38] Zhang, Y.; Wu, B. Q.; He, Y. K.; Deng, W. Y.; Li, J. W.; Li, J. Y.; Qiao, N.; Xing, Y. F.; Yuan, X. Y.; Li, N. et al. Layer-by-layer processed binary all-polymer solar cells with efficiency over 16% enabled by finely optimized morphology. *Nano Energy* **2022**, *93*, 106858.
[39] Lipton, J.; Weng, G. M.; Röhr, J. A.; Wang, H.; Taylor, A. D. Layer-by-layer assembly of two-dimensional materials: Meticulous control on the nanoscale. *Matter* **2020**, *2*, 1148–1165.
[40] Ko, Y.; Park, J.; Mo, J.; Lee, S.; Song, Y.; Ko, Y.; Lee, H.; Kim, Y.; Huh, J.; Lee, S. W. et al. Layer-by-layer assembly-based electrocatalytic fibril electrodes enabling extremely low overpotentials and stable operation at 1 $A \cdot cm^{-2}$ in water-splitting reaction. *Adv. Funct. Mater.* **2021**, *31*, 2102530.
[41] Xiong, P.; Zhang, X. Y.; Wan, H.; Wang, S. J.; Zhao, Y. F.; Zhang, J. Q.; Zhou, D.; Gao, W. C.; Ma, R. Z.; Sasaki, T. et al. Interface modulation of two-dimensional superlattices for efficient overall water splitting. *Nano Lett.* **2019**, *19*, 4518–4526.
[42] Zhang, C.; Zhao, J. W.; Zhou, L.; Li, Z. H.; Shao, M. F.; Wei, M. Layer-by-layer assembly of exfoliated layered double hydroxide nanosheets for enhanced electrochemical oxidation of water. *J. Mater. Chem. A* **2016**, *4*, 11516–11523.
[43] Xie, C. L.; Niu, Z. Q.; Kim, D.; Li, M. F.; Yang, P. D. Surface and interface control in nanoparticle catalysis. *Chem. Rev.* **2020**, *120*, 1184–1249.
[44] Cui, Y. L. S.; Tan, X.; Xiao, K. F.; Zhao, S. L.; Bedford, N. M.; Liu, Y. F.; Wang, Z. C.; Wu, K. H.; Pan, J.; Saputera, W. H. et al. Tungsten oxide/carbide surface heterojunction catalyst with high hydrogen evolution activity. *ACS Energy Lett.* **2020**, *5*, 3560–3568.
[45] Yu, J. F.; Martin, B. R.; Clearfield, A.; Luo, Z. P.; Sun, L. Y. One-step direct synthesis of layered double hydroxide single-layer nanosheets. *Nanoscale* **2015**, *7*, 9448–9451.
[46] Zhao, Y. F.; Zhang, X.; Jia, X. D.; Waterhouse, G. I. N.; Shi, R.; Zhang, X. R.; Zhan, F.; Tao, Y.; Wu, L. Z.; Tung, C. H. et al. Sub-3 nm ultrafine monolayer layered double hydroxide nanosheets for electrochemical water oxidation. *Adv. Energy Mater.* **2018**, *8*, 1703585.
[47] Stevens, M. B.; Enman, L. J.; Batchellor, A. S.; Cosby, M. R.; Vise, A. E.; Trang, C. D. M.; Boettcher, S. W. Measurement techniques for the study of thin film heterogeneous water oxidation electrocatalysts. *Chem. Mater.* **2017**, *29*, 120–140.
[48] Chen, Y. P.; Zhou, Q.; Zhao, G. Q.; Yu, Z. W.; Wang, X. L.; Dou, S. X.; Sun, W. P. Electrochemically inert $g\text{-}C_3N_4$ promotes water oxidation catalysis. *Adv. Funct. Mater.* **2018**, *28*, 1705583.
[49] Anantharaj, S.; Ede, S. R.; Karthick, K.; Sankar, S. S.; Sangeetha, K.; Karthik, P. E.; Kundu, S. Precision and correctness in the evaluation of electrocatalytic water splitting: Revisiting activity parameters with a critical assessment. *Energy Environ. Sci.* **2018**, *11*, 744–771.
[50] Lin, H. W.; Raja, D. S.; Chuah, X. F.; Hsieh, C. T.; Chen, Y. A.; Lu, S. Y. Bi-metallic MOFs possessing hierarchical synergistic effects as high performance electrocatalysts for overall water splitting at high current densities. *Appl. Catal. B:Environ.* **2019**, *258*, 118023.
[51] Wei, C.; Rao, R. R.; Peng, J. Y.; Huang, B. T.; Stephens, I. E. L.; Risch, M.; Xu, Z. J.; Shao-Horn, Y. Recommended practices and benchmark activity for hydrogen and oxygen electrocatalysis in water splitting and fuel cells. *Adv. Mater.* **2019**, *31*, 1806296.
[52] Mei, Y.; Zhou, J. H.; Hao, Y. T.; Hu, X.; Lin, J.; Huang, Y. X.; Li, L.; Feng, C. G.; Wu, F.; Chen, R. J. High-lithiophilicity host with micro/nanostructured active sites based on wenzel wetting model for dendrite-free lithium metal anodes. *Adv. Funct. Mater.* **2021**, *31*, 2106676.
[53] Hou, J. G.; Wu, Y. Z.; Zhang, B.; Cao, S. Y.; Li, Z. W.; Sun, L. C. Rational design of nanoarray architectures for electrocatalytic water splitting. *Adv. Funct. Mater.* **2019**, *29*, 1808367.
[54] Wang, C. P.; Kong, L. J.; Sun, H.; Zhong, M.; Cui, H. J.; Zhang, Y. H.; Wang, D. H.; Zhu, J.; Bu, X. H. Carbon layer coated Ni_3S_2/MoS_2 nanohybrids as efficient bifunctional electrocatalysts for overall water splitting. *ChemElectroChem* **2019**, *6*, 5603–5609.